



# The production of diesel-like hydrocarbons from palmitic acid over HZSM-22 supported nickel phosphide catalysts

Yinghua Liu, Lu Yao, Hui Xin, Guishuo Wang, Dan Li\*, Changwei Hu\*

Key Laboratory of Green Chemistry and Technology, Ministry of Education, College of Chemistry, Sichuan University, Chengdu, Sichuan 610064, PR China

## ARTICLE INFO

### Article history:

Received 19 December 2014

Received in revised form 17 February 2015

Accepted 15 March 2015

Available online 17 March 2015

### Keywords:

Decarbonylation-decarboxylation

Fatty acid

Heterogeneous catalysis

High heat value

*in situ* DRIFTS

## ABSTRACT

We have synthesized the nickel phosphides supported on the commercial HZSM-22 catalysts, which were used to convert palmitic acid to diesel-like hydrocarbons under ambient pressure in the absence of any solvents. The deoxygenation reactions of palmitic acid were studied in a fixed-bed reactor over HZSM-22, Ni<sub>x</sub>P/HZSM-22, Ni<sub>2</sub>P/HZSM-22, the unsupported Ni<sub>x</sub>P and the unsupported Ni<sub>12</sub>P<sub>5</sub> catalysts. The conversion of palmitic acid and the hydrocarbon yield were found to be 99.6% and 42.9%, respectively, for the best catalyst, 40 Ni<sub>x</sub>P/HZSM-22. The heat value of the resulting hydrocarbons was 46.4 MJ kg<sup>-1</sup>. Ketones and aldehydes were identified as reaction intermediates, which were subsequently converted into hydrocarbons. In addition, short-chain hydrocarbons and aromatic hydrocarbons were generated, suggesting the presence of cracking and isomerization reactions. Our mechanistic exploration and the NH<sub>3</sub> adsorption-desorption DRIFT spectra suggest that the decarbonylation and decarboxylation are facilitated by Ni<sub>x</sub>P, whereas Brønsted acid sites on HZSM-22 play a crucial role in the isomerization reactions and Lewis acids sites on catalysts are responsible for the cracking reactions. The present study demonstrates that the catalysts such as Ni<sub>x</sub>P supported on commercial HZSM-22 can serve as a practical modus with excellent catalytic activity to produce diesel-like hydrocarbons from biomass-based oil.

© 2015 Elsevier B.V. All rights reserved.

## 1. Introduction

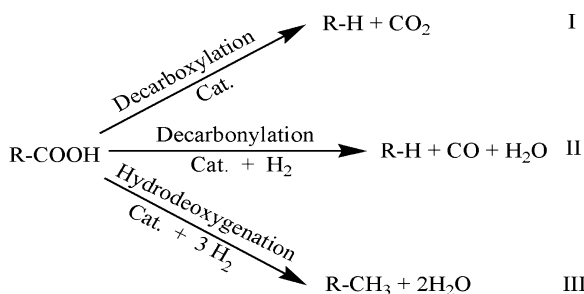
Increased attention has been focused on the effective utilization of biomass, which appears to be an important renewable energy source [1–5]. Fatty acid methyl ester (FAME), obtained by transesterification of triglycerides and/or by esterification of fatty acids, has been extensively studied because of its high lubricity, non-toxicity and renewability [6]. However, FAME has many drawbacks compared to conventional petroleum-derived fuels, such as a relatively high oxygen content, which leads to a relatively poor calorific value, low stability, and high viscosity [7]. Accordingly, the removal of oxygen from biomass-based oil is crucial in the production of high-grade fuels. Fatty acids with long carbon chains (C<sub>16</sub>–C<sub>22</sub>) have been identified as model compounds to investigate the deoxygenation of biomass-based oil.

Currently, three approaches have been used to remove oxygen from fatty acids as shown in **Scheme 1** [7–9], in which the degree of consumption of H<sub>2</sub> follows the order of decarboxylation < decarbonylation < hydrodeoxygenation (**Scheme 1**). Researchers have attempted heterogeneous catalysis to convert fatty acids and their derivatives to fuel range hydrocarbons. Mäki-

Arvela and co-workers reported the decarboxylation of stearic acid, ethyl stearate, and tristearin with a Pd/C catalyst in a semi-batch reactor at 300–360 °C and 0.6–2.7 MPa. The C-supported Pd catalyst was found to facilitate better decarboxylation activity compared to C-supported Pt, Ni, Rh, Ir, Ru, and Os. Mäki-Arvela and co-workers declared that the degree of metal loading played an important role in the fatty acid deoxygenation, with 5 wt% Pd/C found to be an effective catalyst [10–13]. Immer et al. documented that the 5 wt% Pd/C catalyst under He assisted the deoxygenation of stearic acid primarily via decarboxylation, whereas that of oleic acid occurred via decarbonylation [8]. The mechanisms of the catalytic deoxygenation of saturated and unsaturated fatty acids by a Pt/C catalyst were also suggested to be different by Fu et al. [14]. Although supported Pd and Pt catalysts have been found to be effective in the conversion of fatty acids, as well as their derivatives, to diesel-like hydrocarbons, their high cost has encouraged the consecutive development of the low-cost substitutes. According to the activity trends of Pd > Pt > Ni > Rh > Ir > Ru > Os, Snåre et al. have suggested Ni-based catalysts could be promising candidates [13]. Interestingly, Santillan-Jimenez and co-workers compared the catalytic deoxygenation of triglycerides and fatty acids by supported Ni, Pd, and Pt catalysts [6,15]. Among the 20 wt% Ni/C, 5 wt% Pd/C, and 1 wt% Pt/C catalysts studied, the 20 wt% Ni/C showed the highest activity for both cracking of the fatty acid chains and deoxygenation of the triglyceride. Accordingly, when the Ni content is high

\* Corresponding authors. Tel.: +86 2885411105; fax: +86 2885411105.

E-mail addresses: [Danli@scu.edu.cn](mailto:Danli@scu.edu.cn) (D. Li), [changweihu@scu.edu.cn](mailto:changweihu@scu.edu.cn) (C. Hu).



**Scheme 1.** The three pathways proposed for the deoxygenation of a fatty acid into hydrocarbons. The degree of consumption of H<sub>2</sub> follows the order of decarboxylation (I)<decarbonylation (II)<hydrodeoxygenation (III).

enough, Ni-based catalysts could afford better results than Pd or Pt catalysts.

Transition metal phosphides and noble metals show similar chemical properties. Recently, Many scholars reported Ni<sub>2</sub>P as a deoxygenation catalyst [16,17]. Both Ni<sub>2</sub>P/SBA-15 and Ni/SBA-15 exhibited catalytic performance toward the deoxygenation of methyl oleate, in which the former led to a higher n-C<sub>18</sub>/n-C<sub>17</sub> ratio than the latter. (It is worth noting that the C<sub>18</sub> hydrocarbon is the preferred product.) Furthermore, the former favored decarboxylation, whereas the latter assisted both decarboxylation and cracking. Thus, Ni<sub>2</sub>P/SBA-15 was suggested to be a promising catalyst for the production of green diesel [17]. Moreover, the high deoxygenation activity of Ni<sub>2</sub>P/SiO<sub>2</sub> in the catalytic pyrolysis of natural algae was documented by Zeng et al. [18]. Based on the fact that long chain

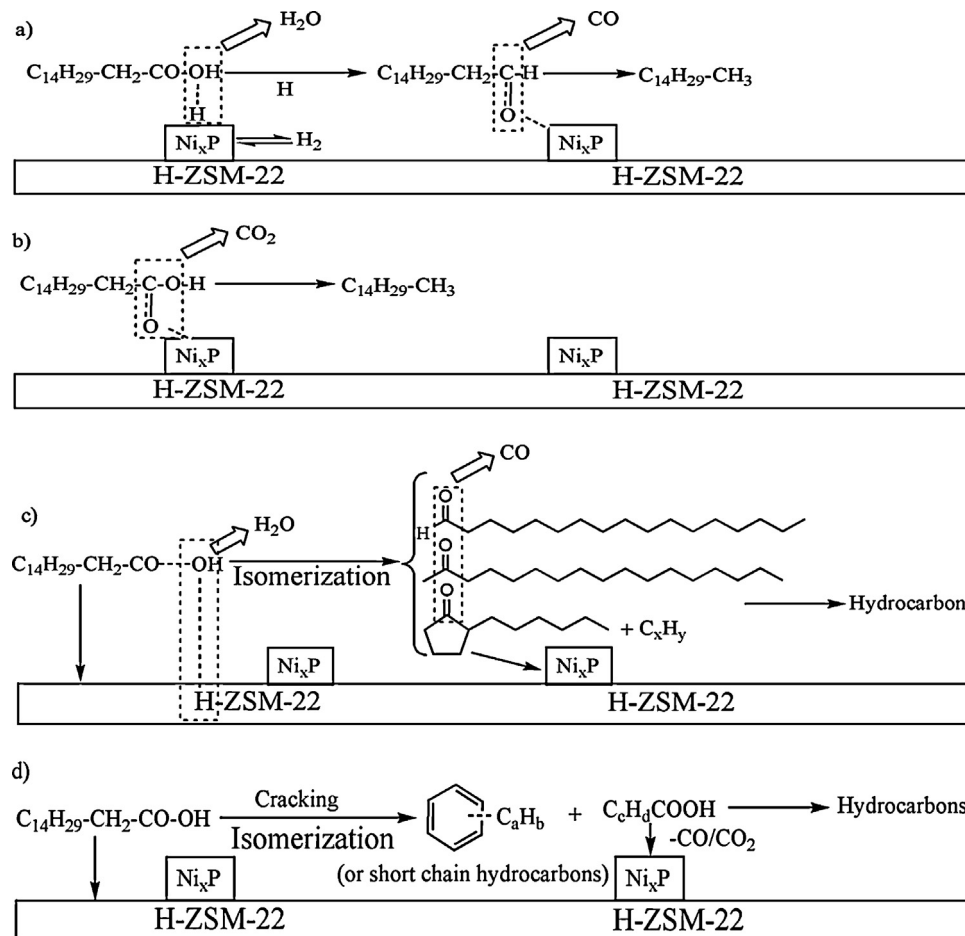
alkanes are the major products of these catalytic deoxygenation processes [17,18], these catalysts exhibit poor performance at low temperatures because of their high pour and cloud points. Fortunately, as demonstrated by Wang et al., a simultaneous catalytic deoxygenation and isomerization process can produce high quality diesel [7]. Diesel-range alkanes have been produced from vegetable oil via Pt/zeolite catalysts.

Herein, we report our efforts on the synthesis of a series of Ni<sub>x</sub>P/HZSM-22 catalysts, Ni<sub>12</sub>P<sub>5</sub> and Ni<sub>2</sub>P supported on HZSM-22 (shown in **Scheme 2**). Additionally, we address their powerful catalytic effects by integrating deoxygenation, cracking and isomerization processes during the conversion of palmitic acid to high-grade diesel (with fuel range hydrocarbons). Finally, we discuss the mechanism of our catalytic deoxygenation, based on *in situ* diffuse reflectance infrared fourier-transform spectroscopy (DRIFTS) and various control experiments. Ni<sub>x</sub>P is argued to be responsible for the decarbonylation and decarboxylation, whereas Brønsted acid sites on HZSM-22 plays a crucial role in the isomerization reactions [7] and Lewis acid sites in the cracking reactions. Our study provides insights into the synthesis of a new generation of catalyst that integrate deoxygenation, cracking and isomerization to convert biomass-based oil into high-quality diesel.

## 2. Experimental

### 2.1. Catalyst preparation and activity test

Commercially available HZSM-22 (with a BET surface area of 194 m<sup>2</sup> g<sup>-1</sup> and Si/Al ratio of 70) was used as the catalyst



**Scheme 2.** The four catalytic pathways proposed for the deoxygenation of palmitic acid on 40NiPZ. Ni<sub>x</sub>P represents Ni<sub>12</sub>P<sub>5</sub> and Ni<sub>2</sub>P. The four pathways are (a) decarbonylation, (b) decarboxylation, (c) initial isomerization, and (d) initial isomerization and cracking.

support. The synthesis of the catalysts involved two stages. First, the precursors were obtained by the incipient wetness impregnation method. HZSM-22 was incipiently impregnated with an aqueous solution containing  $\text{NH}_4\text{H}_2\text{PO}_4$  and  $\text{Ni}(\text{NO}_3)_2 \cdot 6\text{H}_2\text{O}$  with a molar ratio of  $\text{Ni}/\text{P}=2/1$  for 24 h. The loading of  $\text{Ni}_x\text{P}$  was controlled to 5, 20, 40, and 60 wt%. Then, the samples were dried at 100 °C for 12 h and calcined at 600 °C for 4 h [16,19]. Unsupported  $\text{Ni}_x\text{P}$  catalyst was prepared by adding certain amounts of  $\text{NH}_4\text{H}_2\text{PO}_4$  (4.7 g) and  $\text{Ni}(\text{NO}_3)_2 \cdot 6\text{H}_2\text{O}$  (23.5 g) to an appropriate amount of deionized water (approximately 50 mL). The solution was dried at 120 °C for 24 h and calcined at 600 °C for 4 h. Secondly, the catalysts were obtained by reduction of the precursors in flowing  $\text{H}_2$  (30 mL min<sup>-1</sup>). The reduction temperature was increased from room temperature to 600 °C at a rate of 2 °C min<sup>-1</sup> and then maintained for 2 h. The loading was calculated by Eq. (1):

$$\text{Wt\%} = (\text{weight of Ni} + \text{P}) / \text{weight of HZSM-22} \times 100\% \quad (1)$$

The activities of the catalysts were studied in a fixed-bed reactor in the temperature ranged of 310–360 °C. For each run, 1.5 g of palmitic acid was used. The catalyst (3.0 g) was mixed with  $\text{SiO}_2$  to improve heat transfer and ensure a sufficient catalyst-bed length of 4 cm [20]. The carrier gas was 5%  $\text{H}_2/\text{Ar}$  with a flow rate of 30 mL min<sup>-1</sup>. The experimental device (Fig. S1 in the Supporting information) are mainly consisted of a globular quart chamber, a four-way chamber, an outer tube, an inner tube, an electric oven, a liquid products receiver, an ice-water bath, a gas products receiver, a thermoelectric couple, four switches, and rubber hoses. The outer and inner tubes were made of quartz. The globular quart chamber was used for the storage of palmitic acid during the reduction of the catalyst. The outer tube was used to provide and guarantee a  $\text{H}_2$  atmosphere. The catalyst (mixed with  $\text{SiO}_2$ ) was placed on the quartz sand core in the outer tube. The bowl at the bottom of the inner tube provided an evaporation chamber for palmitic acid. The downstream volatiles from the evaporation of the palmitic acid passed through the catalyst bed. There is a very short distance between the bowl of the inner tube and the catalyst to ensure that the catalytic reaction takes place in the thermostatic region of the oven, and the volatiles of palmitic acid can contact the catalyst as soon as possible after evaporation.

## 2.2. Product analysis

The liquid products were qualitatively analyzed by a gas chromatography mass spectrometer (GC-MS, Agilent 5973) equipped with a capillary column (HP-INNOWAX, 30 m × 0.25 mm × 0.25 μm). The gaseous products were also qualitatively analyzed using a GC-MS (Agilent 5975) equipped with a capillary column (Gas Pro 30 m × 0.35 mm).

The liquid products were quantitatively analyzed with a gas chromatograph (GC, FULI 9750) equipped with a capillary column (HP-5, 30 m × 0.25 mm × 0.25 μm) and a flame ionization detector (FID) and  $\text{N}_2$  was used as the carrier gas. The injector and detector temperatures were both 280 °C. The following temperature program was used for the analysis: 70 °C (3 min), 5 °C min<sup>-1</sup>, 160 °C (3 min), 10 °C min<sup>-1</sup>, 230 °C (6 min).

The heat values of the palmitic acid and hydrocarbons were measured by an SHR-15B heat of combustion experiment device at room temperature, and the pressure of oxygen used was 2 MPa.

The conversion ( $X$ ) of palmitic acid was calculated by Eq. (2):

$$X = (W_1 - W_2) / W_1 \times 100\% \quad (2)$$

where  $W_1$  and  $W_2$  are the weights of added and unconverted palmitic acid, respectively.

Hydrocarbon yield (yield) was calculated by Eq. (3):

$$\text{Yield} = (W_{\text{Products}} - W_{\text{water}}) / (W_1 - W_2) \times 100\% \quad (3)$$

where  $W_{\text{Products}}$  and  $W_{\text{water}}$  are the weights of the total products and water generated in the reaction, respectively.

## 2.3. Catalyst characterization

$\text{N}_2$  physisorption isotherms of the samples were measured at -196 °C on a Micromeritics ASAP-2020 analyzer. The surface areas were determined by the Brunauer–Emmett–Teller (BET) equation. The pore volumes and average pore diameters were determined by the Barrett–Joyner–Halenda (BJH) method from the desorption branches of the isotherms.

X-Ray Diffraction (XRD) patterns of the samples were obtained by a DX-1000 X-ray diffractometer using Cu-K $\alpha$  radiation ( $\lambda = 1.542 \text{ \AA}$ ) operating at 40 kV and 25 mA. Powder diffraction profiles were recorded at a 0.06 s<sup>-1</sup> scanning speed over a 2θ range of 3–80°.

Temperature-programmed reduction ( $\text{H}_2$ -TPR) was used to characterize the precursor. The sample (0.1 g) was placed in a fixed-bed reactor and pretreated at 200 °C for 30 min in  $\text{N}_2$  with a flow rate of 30 mL min<sup>-1</sup>. After the temperature was decreased to 80 °C, the sample was heated from 80 to 830 °C with a ramp of 5 °C min<sup>-1</sup> in a 5%  $\text{H}_2/\text{Ar}$  flow. The consumption of  $\text{H}_2$  was analyzed by a GC equipped with a thermal conductivity detector (TCD).

Transmission electron microscopy (TEM) images of the samples were obtained on an FEI company Tecnai G2 20 Twin instrument equipped with an EDX spectrometer and operated at an acceleration voltage of 200 kV.

X-Ray photoelectron spectroscopy (XPS) analysis of the samples was performed on an AXIS Ultra DLD (KRATOS) spectrometer. A monochromatic X-ray source of Al-K $\alpha$  was used as the excitation source and the binding energy (BE) was calibrated using C1s at 284.6 eV. A Shirley background was subtracted from all spectra and peak fitting was performed using an 80/20 Lorentz–Gauss function.

*In situ* DRIFTS was performed from 1250 to 3500 cm<sup>-1</sup> at a spectral resolution of 4 cm<sup>-1</sup> (number of scans, 32) on a Nicolet 5700 FT-IR spectrometer equipped with a high sensitivity MCT detector. The DRIFTS cell (Harrick) was fitted with a ZnSe window and a heating cartridge that allowed the sample to be heated to 400 °C. The catalyst was pretreated with a high purity  $\text{N}_2$  stream at 350 °C for 1 h to eliminate physisorbed water and other impurities. The background of each target temperature was collected during the cooling process of the catalyst. Then, the palmitic acid was placed on the catalyst powder and the spectra were collected at different temperatures. A schematic procedure of the *in situ* DRIFTS is shown in Figs. S2 and S3 in the Supporting information.

$\text{NH}_3$ -temperature programmed desorption ( $\text{NH}_3$ -TPD) experiments were performed using a multifunction chemisorption analyzer. About 0.1 g sample was pretreated in highly purified  $\text{N}_2$  flow (40 mL min<sup>-1</sup>) at 500 °C for 1 h. After pretreatment, the sample was saturated with 1 vol.%  $\text{NH}_3$  (10 mL min<sup>-1</sup>) at 100 °C for 1 h and subsequently flushed with highly purified  $\text{N}_2$  flow at the same temperature for 1 h to remove gaseous and weakly adsorbed  $\text{NH}_3$ , and then the sample was heated to 500 °C at a rate of 10 °C min<sup>-1</sup> in the flowing highly purified  $\text{N}_2$  (40 mL min<sup>-1</sup>). *In situ* DRIFTS  $\text{NH}_3$  adsorption-desorption experimental procedure was similar to the  $\text{NH}_3$ -TPD.

## 3. Results and discussion

Commercial HZSM-22 was used as support for catalyst preparation. A series of  $\text{Ni}_x\text{P}/\text{HZSM-22}$  catalysts were prepared by an incipient impregnation method. According to the content of Ni and P used, the precursors are labeled 5NiPZ-P, 20NiPZ-P, 40NiPZ-P and 60NiPZ-P. The precursors were subjected to  $\text{H}_2$  reduction at 600 °C for 2 h, producing the catalysts 5NiPZ, 20NiPZ, 40NiPZ and

**Table 1**  
Physicochemical properties of the catalysts.

Sample	BET surface area [ $\text{m}^2 \text{ g}^{-1}$ ]	Micropore volumes [ $\text{cm}^3 \text{ g}^{-1}$ ]	Average pore diameter [nm]	$d_{\text{XRD}}$ [nm] <sup>a</sup>	
				$\text{Ni}_2\text{P}$	$\text{Ni}_{12}\text{P}_5$
HZSM-22	194	0.060	6.52	nd <sup>b</sup>	nd
5NiPZ	421	0.041	8.27	nd	12.0
20NiPZ	113	0.019	8.90	20.6	17.3
40NiPZ	75	0.011	10.20	26.3	21.6
60NiPZ	66	0.010	11.51	35.4	23.9
$\text{Ni}_x\text{P}$	13	—	25.24	97.5	—

<sup>a</sup> Crystallite sizes were calculated from the XRD patterns of the catalysts by Scherrer equation.  
<sup>b</sup> nd: the species was not detected.

60NiPZ, respectively. The effect of the supported  $\text{Ni}_x\text{P}$ , on the catalytic deoxygenation of palmitic acid was also compared to that of unsupported  $\text{Ni}_x\text{P}$ . The precursor to prepare the unsupported  $\text{Ni}_x\text{P}$  is labeled as  $\text{Ni}_x\text{P}-\text{P}$ .

### 3.1. Catalyst characterization

The textural properties of the HZSM-22 support and the catalysts were obtained from  $\text{N}_2$  adsorption–desorption isotherms, and the values of different parameters are summarized in Table 1. All of the catalysts possessed type IV sorption isotherms (see Fig. S4 in the Supporting information). HZSM-22 zeolites are typical microporous materials with pore diameters of approximately  $0.46 \times 0.57 \text{ nm}$  [7]. The pore size distribution of HZSM-22 and the micropore volumes of the precursors are provided in Fig. S5 and Table S1 in the Supporting information. As shown in Table 1, both the BET surface area and the micropore volumes gradually decreased with increasing Ni and P loading, whereas the average pore diameter gradually increased. These results indicated that the small crystals ( $d < 0.68 \text{ nm}$ ) of  $\text{Ni}_x\text{P}$  may enter into the pore of HZSM-22 or even block the small pores.

Fig. 1 shows the XRD patterns of unsupported  $\text{Ni}_x\text{P}-\text{P}$ , 60NiPZ-P, 40NiPZ-P, 20NiPZ-P, 5NiPZ-P, and HZSM-22. The XRD patterns of 5NiPZ-P and 20NiPZ-P were similar to that of HZSM-22 support, in which only the characteristic peaks of HZSM-22 were observed,

suggesting that the nickel and phosphate species were highly dispersed on HZSM-22. When the loading of Ni and P increased, the XRD of 40NiPZ, 60NiPZ, and unsupported  $\text{Ni}_x\text{P}$  presented the characteristic peaks of  $\text{NiO}$  (PDF#65-5745) at  $37.6^\circ$ ,  $43.6^\circ$ , and  $63.2^\circ$ . The results were in agreement with the literature [18].

Fig. 2 shows the XRD patterns of all the reduced NiPZ catalysts, unsupported  $\text{Ni}_x\text{P}$  and HZSM-22 support. The crystallite sizes of  $\text{Ni}_2\text{P}$  and  $\text{Ni}_{12}\text{P}_5$  were calculated by the Scherrer equation, the results of which are shown in Table 1. The XRD patterns of the unsupported  $\text{Ni}_x\text{P}$  were similar to the powder diffraction file of  $\text{Ni}_2\text{P}$  (PDF#65-9706), where sharp diffraction peaks appeared at  $40.8^\circ$ ,  $44.7^\circ$ ,  $47.3^\circ$ ,  $54.2^\circ$ ,  $55.1^\circ$ ,  $66.5^\circ$ ,  $72.8^\circ$ , and  $74.8^\circ$  [21–23]. For the NiPZ catalysts, the intensity of the diffraction peaks of  $\text{Ni}_x\text{P}$  strengthened with increased loading of Ni and P. The XRD patterns of 5NiPZ was similar to that of the HZSM-22 support, in which only a weak diffraction peak assigned to  $\text{Ni}_{12}\text{P}_5$  (PDF#22-1190) ( $41.3^\circ$ ) was observed. For 20NiPZ, the diffraction peaks appearing at  $35.8^\circ$ ,  $38.5^\circ$ ,  $41.3^\circ$ ,  $47.1^\circ$ , and  $49.1^\circ$  were assigned to  $\text{Ni}_{12}\text{P}_5$  (PDF#22-1190), and the diffraction peak at  $44.7^\circ$  was assigned to  $\text{Ni}_2\text{P}$  (PDF#65-9706). For 40NiPZ, the diffraction peaks of  $\text{Ni}_2\text{P}$  were observed at  $40.8^\circ$ ,  $44.7^\circ$ , and  $54.2^\circ$ , and the intensity of the  $\text{Ni}_{12}\text{P}_5$  diffraction peaks was strengthened. The crystallite sizes of  $\text{Ni}_2\text{P}$  and  $\text{Ni}_{12}\text{P}_5$  also increased with increasing loading of Ni and P. The crystallite size of  $\text{Ni}_2\text{P}$  increased from 20.6 to 26.3 nm when the loading of Ni and P increased from 20 to 40%, whereas the crystallite size

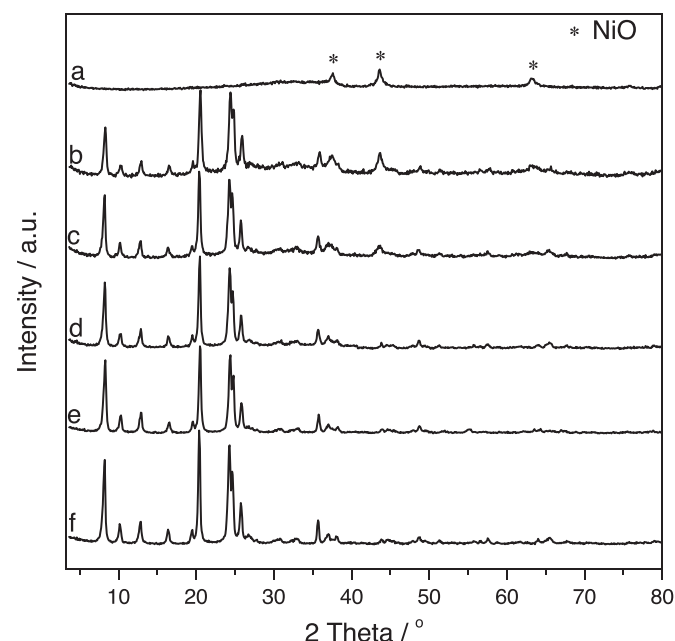


**Fig. 1.** XRD patterns of the precursors (a) unsupported  $\text{Ni}_x\text{P}-\text{P}$ , (b) 60NiPZ-P, (c) 40NiPZ-P, (d) 20NiPZ-P, (e) 5NiPZ-P, and (f) HZSM-22.  $\text{NiO}$  crystals are marked with \*.

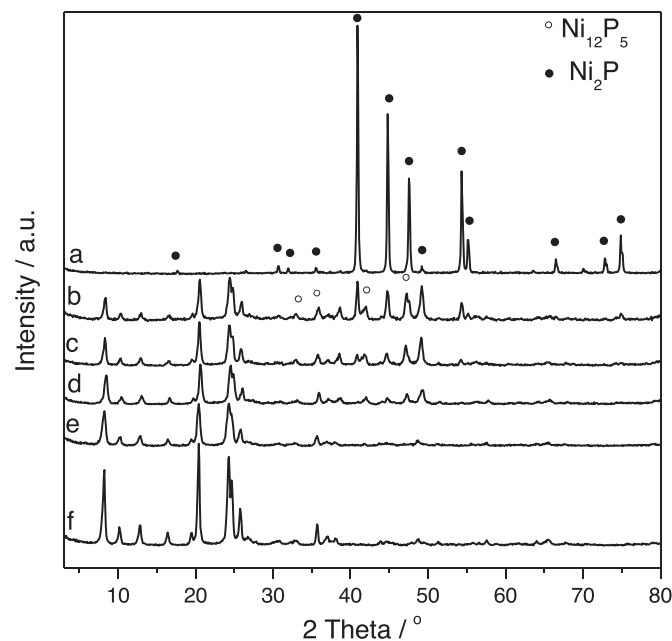


**Fig. 2.** XRD patterns of reduced catalysts (a) unsupported  $\text{Ni}_x\text{P}$ , (b) 60NiPZ, (c) 40NiPZ, (d) 20NiPZ, (e) 5NiPZ, and (f) HZSM-22.  $\text{Ni}_{12}\text{P}_5$  and  $\text{Ni}_2\text{P}$  crystals are marked with ○ and ●, respectively.

$H_2$ Consumption / a.u.

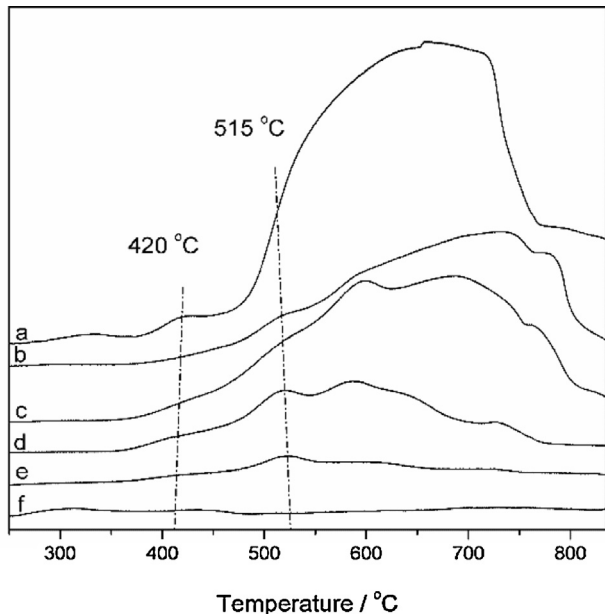


**Fig. 3.**  $H_2$ -TPR traces of the precursors (a) unsupported  $Ni_xP$ -P, (b) 60NiPZ-P, (c) 40NiPZ-P, (d) 20NiPZ-P, (e) 5NiPZ-P, (f) HZSM-22. Temperature range from 250 °C to 830 °C, heating rate 5 °C/min in a 5%  $H_2$ /Ar gas stream.

of  $Ni_{12}P_5$  increased from 12.0 to 21.6 nm with an increase in the Ni and P loading from 5 to 40%. For 60NiPZ, the new diffraction peaks assigned to  $Ni_2P$  (PDF#65-9706) were observed at 47.3° and 55.1°, and the intensity of the  $Ni_2P$  diffraction peaks was strengthened and the crystallite size increased to 35.4 nm. The intensity of the  $Ni_{12}P_5$  diffraction peaks also was strengthened; however, the crystallite size of  $Ni_{12}P_5$  increased to only 23.9 nm (comparing to 21.6 nm for 40NiPZ). This result indicates that  $Ni_2P$  would predominantly form in the absence of HZSM-22, whereas the  $Ni_{12}P_5$  crystalline phase would first form on  $Ni_xP$ /HZSM-22 when the loading of Ni and P was low under the conditions used in the present work. Thus, we inferred that HZSM-22 might induce the formation of  $Ni_{12}P_5$ .

$H_2$ -TPR could provide information about the reduction behavior of the precursors. Fig. 3 presents the  $H_2$ -TPR profiles of the precursors and the HZSM-22 support. For HZSM-22, no obvious reduction peak was observed over the temperature range of 250 to 830 °C. The  $H_2$ -TPR profiles of all the precursors were similar, and the intensity of the reduction peaks strengthened with increasing Ni and P loading. The peaks at approximately 420 and 515 °C were assigned to the reduction of bulk  $NiO$  and  $NiO$  interacting with the support, respectively [24,25]. The peaks at approximately 590–730 °C were ascribed to the reduction of the P–O band [16]. The TPR profile of the unsupported  $Ni_xP$ -P consisted of two main features: one at low temperature and one at high temperature. The first peak at 420 °C was attributed to the reduction of  $NiO$ , whereas the second peak with a maximum at 515–730 °C was assigned to the reduction of the P–O band according to the above results. Therefore,  $Ni_{12}P_5$  and  $Ni_2P$  were formed from the reduction of both  $NiO$  and the P–O band.

To gain deeper insight into the valence state of the Ni and P species in both the precursors and the catalysts, XPS measurements were performed. The XPS spectra in the Ni (2p) and P (2p) regions, for the precursors and the catalysts, are shown in Figs. 4 and 5, respectively. The band intensities of Ni (2p) and P (2p) increased with increasing loading of Ni and P. All spectra were decomposed by taking into account the spin-orbit splitting of Ni (2p<sub>3/2</sub>) and Ni (2p<sub>1/2</sub>) lines (17 eV) and the shake-up peaks at approximately 5 eV higher than the binding energy of the parent signal.

The XPS spectra for the precursors exhibit Ni (2p<sub>3/2</sub>) peaks at approximately 857.1 and 854.1 eV, which could be assigned to  $Ni^{2+}$

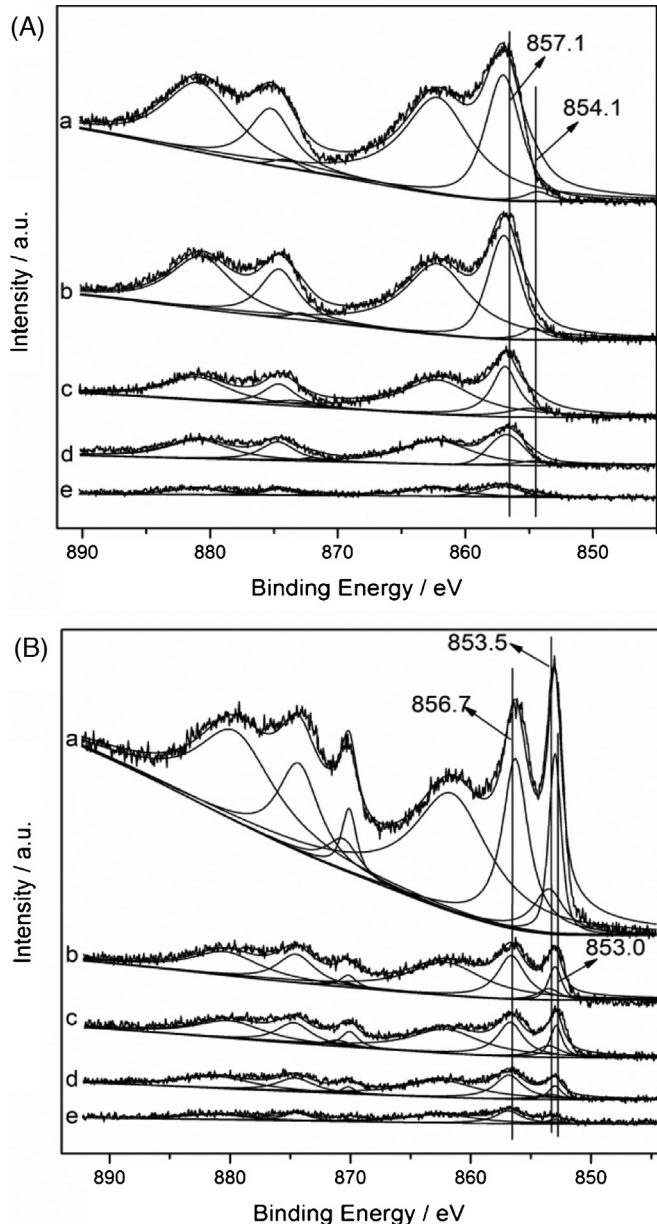


**Fig. 4.** XPS spectra of Ni 2p region for the (A) precursors: (a) unsupported  $Ni_xP$ -P, (b) 60NiPZ-P, (c) 40NiPZ-P, (d) 20NiPZ-P, and (e) 5NiPZ-P and (B) catalysts: (a) unsupported  $Ni_xP$ , (b) 60NiPZ, (c) 40NiPZ, (d) 20NiPZ, and (e) 5NiPZ.

strongly interacting with the support or in  $NiO$ , respectively [26]. The P (2p<sub>3/2</sub>) peak at approximately 133.6 eV was attributed to  $P^{5+}$  in  $PO_4^{3-}$  [27,28]. For the reduced catalysts, the Ni (2p<sub>3/2</sub>) peaks at 853.5 and 853.0 eV were assigned to  $Ni^{3+}$  in  $Ni_2P$  and  $Ni_{12}P_5$ , respectively, whereas the P (2p<sub>3/2</sub>) peak at 129.5 eV was assigned to  $P^{\delta-}$  in  $Ni_2P$  and  $Ni_{12}P_5$  [21,22]. The peaks at 856.7 and 134.4 eV were assigned to  $Ni^{2+}$  and  $P^{5+}$ , respectively, which were derived from the oxidation of the catalysts upon contacting with air [16,21]. These results indicated that nickel phosphides were generated on HZSM-22. Moreover, these binding energies indicated that there was a small electron transfer from Ni to P, in that Ni in nickel phosphide had a partial positive charge ( $\delta+$ ), where  $0 < \delta < 2$ , and the P had a partial negative charge ( $\delta-$ ), where  $0 < \delta < 1$ .

TEM images of HZSM-22, 40NiPZ-P and 40NiPZ are displayed in Fig. 6. The HZSM-22 support was observed to exhibit a stick-shaped structure. For 40NiPZ-P, a number of grains were observed, which were attributed to  $NiO$ . After  $H_2$  reduction, the new crystals were

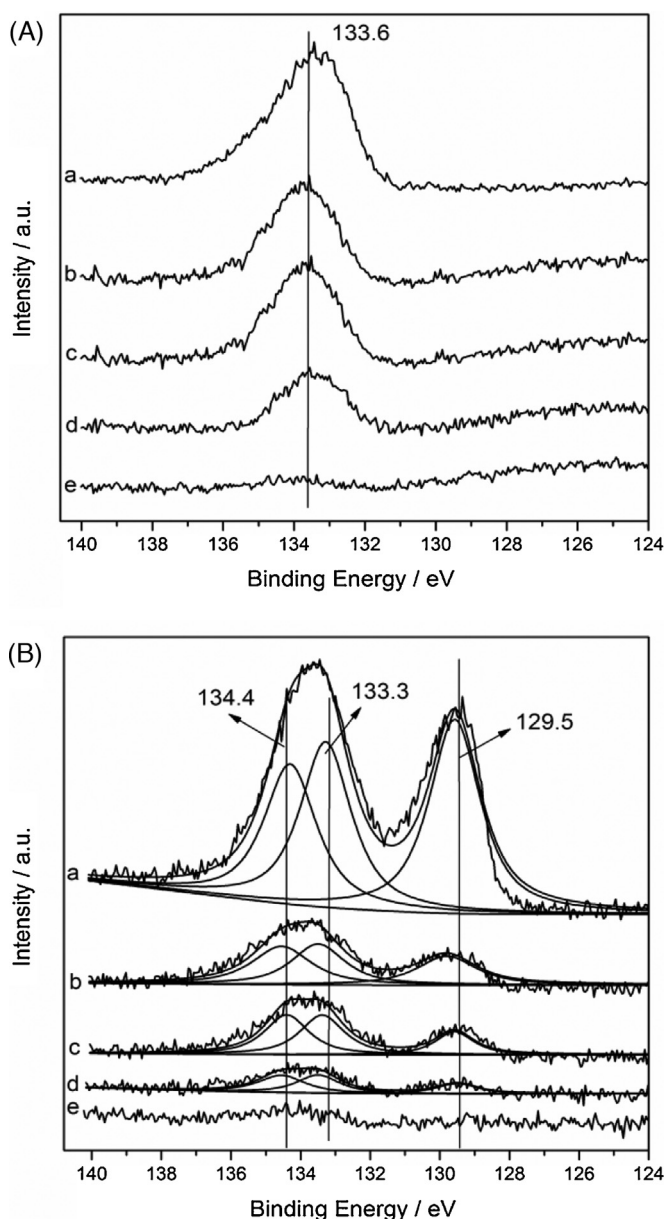


**Fig. 5.** XPS spectra of P 2p region for the (A) precursors: (a) unsupported Ni<sub>x</sub>P-P, (b) 60NiPZ-P, (c) 40NiPZ-P, (d) 20NiPZ-P, and (e) 5NiPZ-P and (B) catalysts: (a) unsupported Ni<sub>x</sub>P, (b) 60NiPZ, (c) 40NiPZ, (d) 20NiPZ, and (e) 5NiPZ.

formed. Gray spots on 40NiPZ containing Ni and P elements were observed by EDX analysis, as shown in Fig. S6 in the Supporting information. Combining with the results of XRD and XPS, the grains were attributed to Ni<sub>12</sub>P<sub>5</sub> and Ni<sub>2</sub>P. In addition, the NiO grains presented more irregular morphologies compared to the Ni<sub>x</sub>P (Ni<sub>12</sub>P<sub>5</sub> and Ni<sub>2</sub>P) grains. The stick-shaped structure was maintained after H<sub>2</sub> treatment at 600 °C for 2 h, indicating the high stability of the support.

TEM images of the NiPZ and unsupported Ni<sub>x</sub>P catalysts are shown in Fig. 7. All of the micrographs exhibited good dispersion of Ni<sub>x</sub>P (Ni<sub>12</sub>P<sub>5</sub> and Ni<sub>2</sub>P) on the HZSM-22 support. The Ni<sub>x</sub>P (Ni<sub>12</sub>P<sub>5</sub> and Ni<sub>2</sub>P) particle sizes increased with the increased loading of Ni and P. It was observed that the Ni<sub>x</sub>P (Ni<sub>2</sub>P) particles aggregated into larger particles in the unsupported Ni<sub>x</sub>P. Based on the TEM results, the particle size distributions of all the NiPZ catalysts were estimated, as shown in Fig. 8. The Ni<sub>x</sub>P (Ni<sub>12</sub>P<sub>5</sub> and Ni<sub>2</sub>P) crystal sizes were calculated with an accuracy of ±1 nm. The analysis indicated

a relatively narrow size distributions in the range of 5–40 nm with a sharp maximum at 5–25 nm for 5NiPZ, and wider distributions in the range of 10–50 nm with a sharp maximum at 15–35 nm for 20NiPZ, 15–65 nm with sharp maximum at 20–45 nm for 40NiPZ, and 15–95 nm with a sharp maximum at 25–55 nm for 60NiPZ, which are in agreement with the  $d_{XRD}$  values calculated from the Scherrer equation. Upon increasing the loading of Ni and P, the Ni<sub>x</sub>P (Ni<sub>12</sub>P<sub>5</sub> and Ni<sub>2</sub>P) particle size distributions with sharp maxima gradually increased.

### 3.2. Catalytic activity

The deoxygenation reactions of palmitic acid over the support, NiPZ catalysts, and unsupported Ni<sub>x</sub>P were performed in a special fixed-bed reactor. The results are shown in Table 2. The conversion of palmitic acid reached 100% over HZSM-22, 5NiPZ, and 20NiPZ, whereas the hydrocarbon yields were only 11.6, 14.0, and 17.3%, respectively. The NH<sub>3</sub>-TPD and NH<sub>3</sub> adsorption-desorption DRIFT (see Figs. S7 and S8 in the Supporting information) results suggested that Lewis acids on HZSM-22, 5NiPZ, and 20NiPZ were the strong acids and beneficial to the cracking reaction to form gaseous products, so the hydrocarbon yields were low. With increased loading of Ni and P, Lewis acids disappeared at 350 °C in the NH<sub>3</sub> adsorption-desorption DRIFT spectra (see Fig. S8 in the Supporting information), and the conversion of palmitic acid decreased slightly to 99.6 and 99.4% over 40NiPZ and 60NiPZ, respectively; however, the hydrocarbon yield increased to 42.9 and 45.7%, respectively. Unsupported Ni<sub>x</sub>P (Ni<sub>2</sub>P) also showed some activity but the conversion of palmitic acid was only 14.2%, which was lower than that of all the NiPZ catalysts. The products collected over the unsupported Ni<sub>x</sub>P catalyst were solid and a large amount of unconverted palmitic acid was observed by GC-MS and GC analysis. If the palmitic acid were converted completely to pentadecane by decarboxylation and decarbonylation, the maximum theoretical hydrocarbon (pentadecane) yield would be 82.8%. In the results shown in Table 2, all of the hydrocarbon yields were lower than the maximum theoretical hydrocarbon yield, mainly as a result of the cracking reaction that occurred on the catalysts. The gaseous products were mainly composed of CO, CO<sub>2</sub>, CH<sub>4</sub>, and C<sub>2</sub>H<sub>6</sub> as determined by GC analysis. Small amounts of other gaseous products, such as propane, propene, butane, (Z)-2-butene ((E)-2-butene), 1-butene and pentane, over the NiPZ catalysts and the HZSM-22 support were also observed by GC-MS. It was noted that the amount of CH<sub>4</sub> in the gaseous products was the highest over HZSM-22, but it decreased with increased loading of Ni and P.

When the Ni and P loading was above 40%, the relative amount of CH<sub>4</sub> did not change significantly. A small amount of CO<sub>2</sub> was detected over HZSM-22 and the amount of CO<sub>2</sub> increased when NiPZ catalysts were used. These results indicated that Lewis acids on HZSM-22 support possessed strong cracking ability, whereas the nickel phosphide was mainly responsible for decarboxylation. By increasing loading of Ni and P, Lewis acids disappeared and the cracking reaction was inhibited, whereas the decarboxylation reaction was enhanced. Additionally, a blank experiment was performed for the deoxygenation reactions of palmitic acid, the results (see Fig. S9 in the Supporting information) of which suggest that SiO<sub>2</sub> is completely inert. Therefore, SiO<sub>2</sub> served only as a dilutant for the catalysts in the deoxygenation reaction. When the reaction temperature reached 350 °C, the palmitic acid decomposed without a catalyst; however, the degree of decomposition was limited.

Based on the results of XRD, when the Ni and P loading increased from 20 to 40%, the crystallite sizes of Ni<sub>2</sub>P and Ni<sub>12</sub>P<sub>5</sub> all increased. The hydrocarbon yield also increased significantly from 17.3 to 42.9%. However, when the Ni and P loading increased from 40 to 60%, the crystallite size of the Ni<sub>2</sub>P increased from 26.3 to 35.4 nm and the crystallite size of Ni<sub>12</sub>P<sub>5</sub> increased from 21.6 to 23.9 nm,

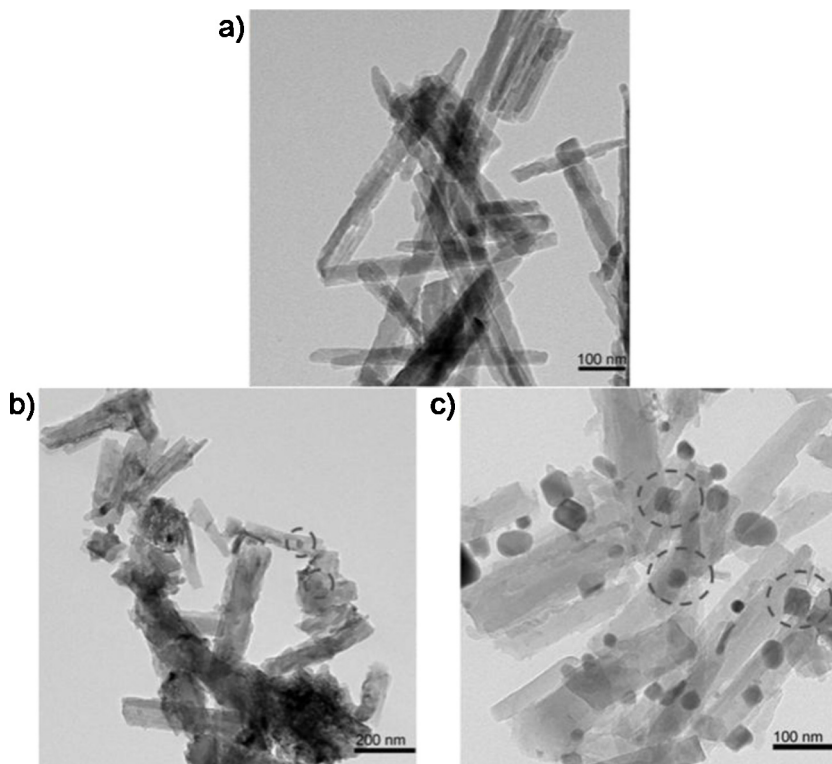


**Fig. 6.** TEM images of (a) HZSM-22, (b) 40NiPZ-P and (c) 40NiPZ catalysts. Scale bars represent 100 nm in images (a) and (c), 200 nm in image (b). After H<sub>2</sub>-reduction, Ni<sub>x</sub>P crystals form in image (c).

whereas the hydrocarbon yield increased slightly. These results indicated that the crystallite size might also play an important role in the conversion of palmitic acid and the subsequent hydrocarbon yield. To study the effect of Ni<sub>2</sub>P and Ni<sub>12</sub>P<sub>5</sub> on the conversion of palmitic acid, the Ni<sub>2</sub>P/HZSM-22 catalyst and the unsupported Ni<sub>12</sub>P<sub>5</sub> were prepared. The amount of Ni controlled in Ni<sub>2</sub>P/HZSM-22 and the unsupported Ni<sub>12</sub>P<sub>5</sub> were the same as that in 40NiPZ. The XRD patterns of Ni<sub>2</sub>P/HZSM-22 and the unsupported Ni<sub>12</sub>P<sub>5</sub> show the formation of Ni<sub>2</sub>P on HZSM-22 and the formation of pure Ni<sub>12</sub>P<sub>5</sub> phase (shown in Fig. S10 in the Supporting information), respectively. The products obtained over the Ni<sub>2</sub>P/HZSM-22 catalyst were solid and the conversion of palmitic acid was only 53.7%, which was lower than 100% conversion on Ni<sub>x</sub>P/HZSM-22 catalysts. The conversion of palmitic acid on the unsupported Ni<sub>x</sub>P (Ni<sub>2</sub>P) and the unsupported Ni<sub>12</sub>P<sub>5</sub> were 14.2% and 92.8%, respectively. Which also suggested that Ni<sub>2</sub>P possesses low activity toward the deoxygenation of palmitic acid, whereas Ni<sub>12</sub>P<sub>5</sub> may be highly active. The crystalline phase of Ni<sub>12</sub>P<sub>5</sub> was proposed to be the main active phase, and the crystallite size of Ni<sub>12</sub>P<sub>5</sub> (within 20–24 nm) was beneficial to the decarboxylation and decarbonylation of palmitic acid, and to the enhancement of hydrocarbon yield.

Based on the above results, 40NiPZ was selected for further study of the temperature effect on the deoxygenation reaction of palmitic acid. Fig. 9 shows the conversion of palmitic acid and hydrocarbon yield as a function of temperature. The conversion of palmitic acid slightly decreased with increasing temperatures from 310 to 360 °C. When the reaction temperature was 310–330 °C, 100% conversion of palmitic acid was obtained and the hydrocarbon yield increased from 20.2 to 37.4%. Upon increasing the temperature from 340 to 360 °C, the conversion of palmitic acid was reduced from 99.8 to 99.4%, whereas the hydrocarbon yield increased from 42.0 to 44.1%. These results indicated that the reaction temperature played an important role in the reaction, in which the hydrocarbon yield tends to remain steady at the temperatures above 340 °C.

### 3.3. Intermediates formed in the conversion of palmitic acid over the HZSM-22 support, 40NiPZ, and unsupported Ni<sub>x</sub>P monitored by in situ DRIFTS

To investigate the mechanism of the deoxygenation of palmitic acid, *in situ* DRIFTS was used to study the reaction over HZSM-22, 40NiPZ, and unsupported Ni<sub>x</sub>P catalysts, the results of which are shown in Fig. 10. The reference DRIFTS spectrum of the reactant (palmitic acid) is compiled in Fig. S11 in the Supporting information. Characteristic absorption peaks of palmitic acid were observed at 2850 cm<sup>-1</sup> ( $\nu$  (-CH<sub>3</sub>)), 2920 cm<sup>-1</sup> ( $\nu$  (-CH<sub>2</sub>)), and 1700 cm<sup>-1</sup> ( $\nu$  (C=O)) [29,29].

Fig. 10(a) shows the *in situ* DRIFTS for the conversion of palmitic acid over the unsupported Ni<sub>x</sub>P catalyst. The peaks at 1690, 2843, and 2914 cm<sup>-1</sup> were attributed to the absorption peaks of palmitic acid. The  $\nu$  (C=O) stretching band in palmitic acid red shifted to 1690 cm<sup>-1</sup>, possibly as a result of the interaction of palmitic acid with the unsupported Ni<sub>x</sub>P catalyst. These peaks exhibited minimal change with increasing temperature. It was noted, however, that a new peak attributed to CO<sub>2</sub> absorption was observed at 2360 cm<sup>-1</sup> when the temperature was increased to above 260 °C [29,30], which indicates that the unsupported Ni<sub>x</sub>P favored CO<sub>2</sub> formation by direct decarboxylation. However, the degree of decarboxylation of palmitic acid was limited.

Over the HZSM-22 support, strong  $\nu$  (C—H) stretching bands were still observed at 2848 and 2920 cm<sup>-1</sup>, as shown in Fig. 10(b). The  $\nu$  (C=O) stretching bands in palmitic acid blue shifted and appeared at 1720 cm<sup>-1</sup>, which may be a result of the interaction of palmitic acid with the support. The bands at 1610–1780 cm<sup>-1</sup> changed markedly with increasing temperature. At 220 °C, a new band at 1757 cm<sup>-1</sup> attributed to the  $\nu$  (C=O) in aldehyde was observed. The aldehyde was formed by the dehydration of palmitic acid on the HZSM-22 support. When the temperature increased to 280 °C, the band at 1720 cm<sup>-1</sup> disappeared and three new

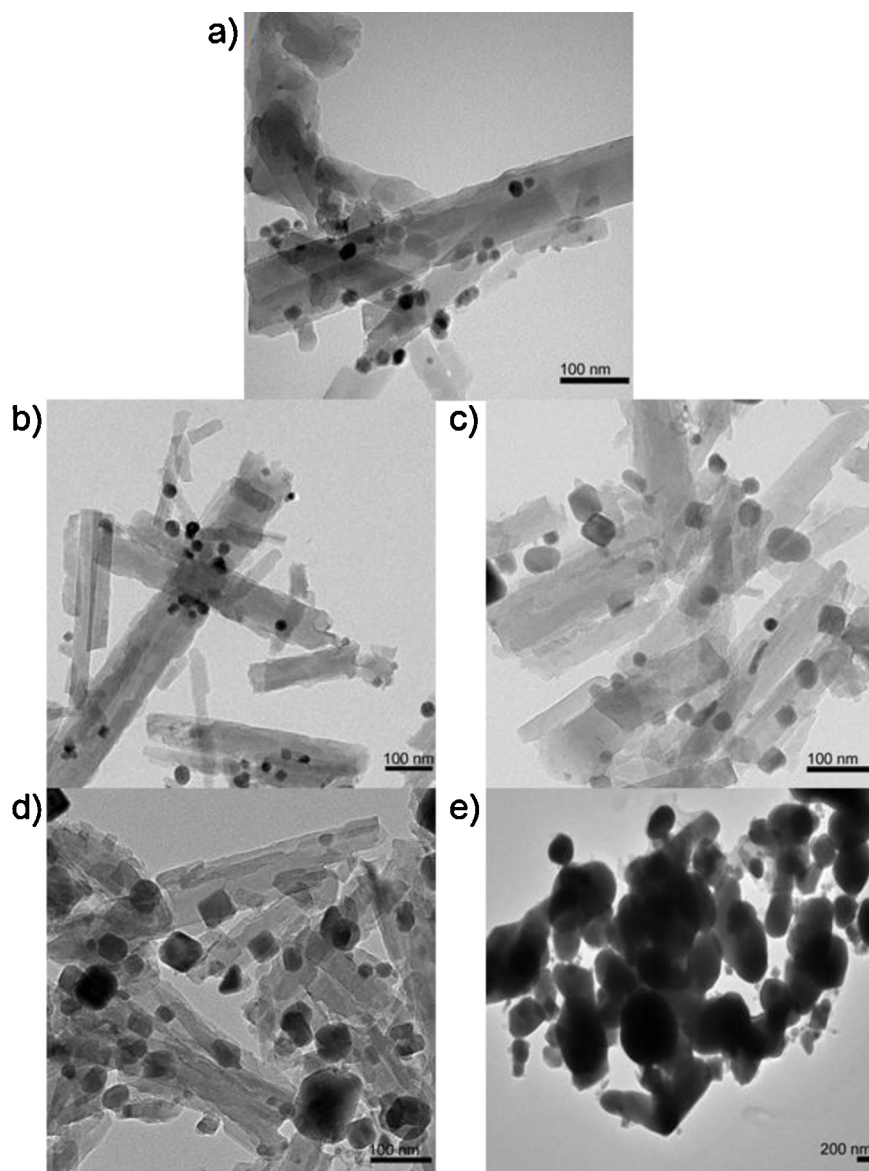


**Fig. 7.** TEM images of different catalysts (a) 5NiPZ, (b) 20NiPZ, (c) 40NiPZ, (d) 60NiPZ, and (e) unsupported  $\text{Ni}_x\text{P}$ .  $\text{Ni}_x\text{P}$  crystals were observed in images (a)–(d), and  $\text{Ni}_2\text{P}$  were observed in image (e).

**Table 2**  
Catalytic performance of different catalysts.<sup>a</sup>

Catalysts	Conversion (%)	Hydrocarbon yield (%) <sup>b</sup>
HZSM-22	100.0	11.6
5NiPZ	100.0	14.0
20NiPZ	100.0	17.3
40NiPZ	99.6	42.9 <sup>c</sup>
60NiPZ	99.4	45.7
$\text{Ni}_x\text{P}$	14.2	—

<sup>a</sup> Reaction conditions: palmitic acid (1.5 g), catalyst (3.0 g),  $T = 350^\circ\text{C}$ ,  $P = 0.1 \text{ MPa}$ , 5%  $\text{H}_2/\text{Ar}$  with a flow rate of  $30 \text{ mL min}^{-1}$ , 2.5 h.

<sup>b</sup> After the reaction, liquid products were collected and analyzed.

<sup>c</sup> The heating value (HV) of hydrocarbon reaches to  $46.4 \text{ MJ kg}^{-1}$ .

bands were observed at  $1650$ ,  $1695$ , and  $1737 \text{ cm}^{-1}$ , which were attributed to the  $\nu(\text{C=O})$  of aromatic ketone, five-membered ring ketone, and long chain fatty ketone, respectively [29]. Ketones were formed by the dehydration of palmitic acid and breakage of the  $\text{C}-\text{C}$  band (in palmitic acid) by the carbonium ion mechanism. First,  $\text{RCO}\cdot$  species are formed by the dehydration of palmitic acid,

which then participate in isomerization reactions on the acid sites of the HZSM-22 support to from ketones. This indicates that isomerization and cracking of palmitic acid occur over the HZSM-22 support because of its Brønsted acid and Lewis acid sites (seen in Fig. S8 in the Supporting information). The intensity of the band at  $1757 \text{ cm}^{-1}$  increased when the temperature was increased from  $220$  to  $260^\circ\text{C}$ ; however, it decreased when the temperature was increased from  $280$  to  $350^\circ\text{C}$  and disappeared at  $350^\circ\text{C}$ . When the temperature was increased from  $280$  to  $350^\circ\text{C}$ , the intensity of the band at  $1650 \text{ cm}^{-1}$  decreased, whereas the intensity of the bands at  $1695$  and  $1737 \text{ cm}^{-1}$  increased. This observation suggests that aldehydes and aromatic ketones are formed in the reaction process, which were not stable, and may be converted into aliphatic ketones and/or cracked over the support. A very weak peak attributed to  $\text{CO}_2$  absorption was observed at  $2360 \text{ cm}^{-1}$  when the temperature was increased above  $260^\circ\text{C}$ , which suggested that the decomposition of palmitic acid might also occur on HZSM-22. However, the reaction proceeded to a very limited extent, which was consistent with the results of the blank experiment (see Fig. S9 in the Supporting information).

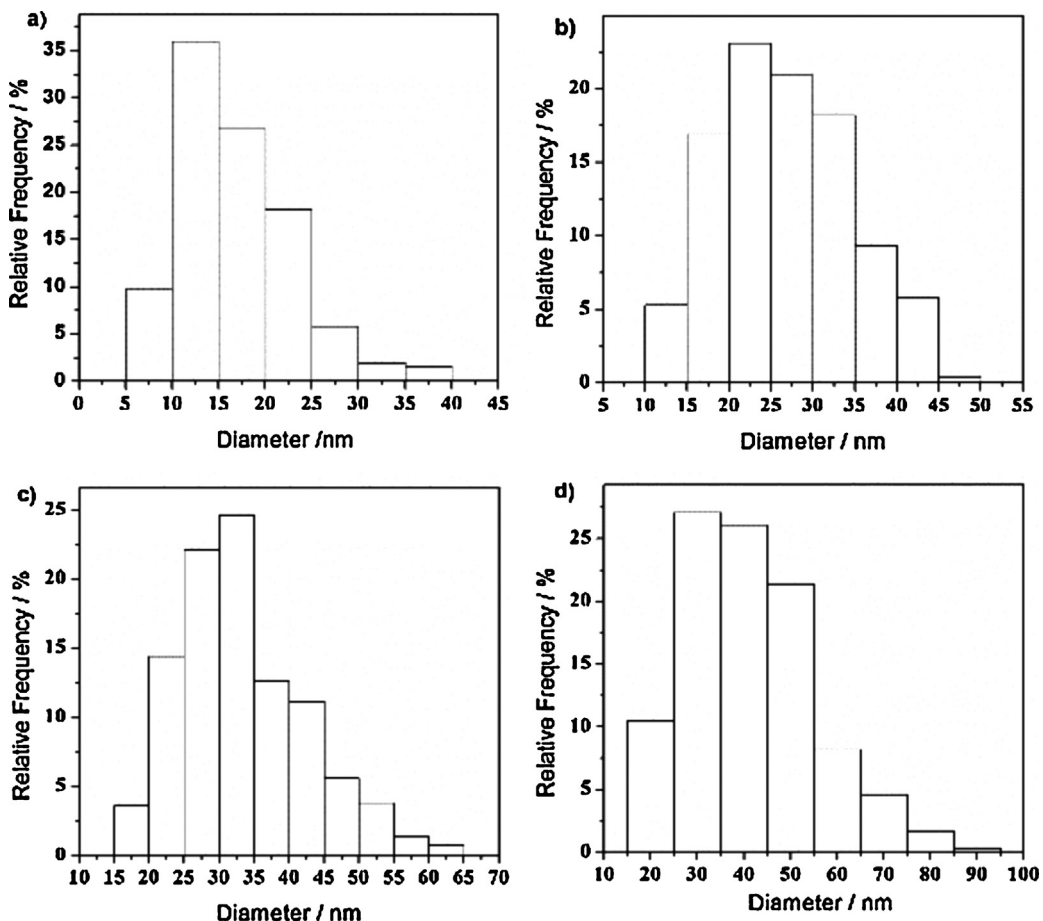


**Fig. 8.** The  $\text{Ni}_x\text{P}$  ( $\text{Ni}_{12}\text{P}_5$  and  $\text{Ni}_2\text{P}$ ) particle size distributions of different catalysts obtained by TEM (a) 5NiPZ, (b) 20NiPZ, (c) 40NiPZ, and (d) 60NiPZ.

The bands at  $1610$ – $1780\text{ cm}^{-1}$  over 40NiPZ, shown in Fig. 10(c) were similar to those obtained over the HZSM-22 support. However, the bands at  $1650$ ,  $1737$ , and  $1757\text{ cm}^{-1}$  disappeared gradually upon increasing the temperature from  $280$  to  $350^\circ\text{C}$ ,

which indicates that ketone and aldehyde intermediates were formed, which were further converted into alkanes by decarbonylation over 40NiPZ. Aldehydes were formed by dehydration of palmitic acid on HZSM-22 and  $\text{Ni}_x\text{P}$  catalysts. The band at  $1695\text{ cm}^{-1}$  still existed and its intensity decreased gradually with increasing temperature from  $280$  to  $350^\circ\text{C}$ . The band at  $1695\text{ cm}^{-1}$  also blue shifted with increasing perature and appeared at  $1700\text{ cm}^{-1}$  when the temperature increased to  $350^\circ\text{C}$ . The new band at  $2360\text{ cm}^{-1}$  attributed to  $\text{CO}_2$  absorption appeared above  $260^\circ\text{C}$  over 40NiPZ, indicating the occurrence of decarboxylation.

All of the *in situ* DRIFTS and  $\text{NH}_3$  adsorption–desorption DRIFT results indicated that  $\text{Ni}_x\text{P}$  ( $\text{Ni}_{12}\text{P}_5$  and  $\text{Ni}_2\text{P}$ )-based catalysts favor decarboxylation and decarbonylation, whereas Brønsted acid sites on HZSM-22 support was proposed to be mainly responsible for the isomerization reactions [7] and Lewis acid sites for the cracking reactions. The mechanism of isomerization will be further investigated in the future. Furthermore, it was deduced that ketones and aldehydes were produced as intermediates in the deoxygenation of palmitic acid. These results differ from those reported by Peng et al. [9], in which obvious  $\nu(\text{C}=\text{C}=\text{O})$  stretching bands were observed at  $2050$ – $2150\text{ cm}^{-1}$ , which were attributed to the IR spectrum of ketene. Thus, ketene was thought to be an important intermediate with  $\text{Ni}/\text{ZrO}_2$  and  $\text{ZrO}_2$  catalysts because of the strong adsorption of palmitic acid at the oxygen vacancy sites of  $\text{ZrO}_2$ .

To further confirm the existence of ketones and aldehydes as intermediates, the control experiments were designed and performed over 40NiPZ, the results of which are shown in Fig. 11. To control the degree of the reaction, different catalyst dosages were employed. When the catalyst dosage was  $1.0\text{ g}$ , palmitic acid was not completely converted. The liquid products were

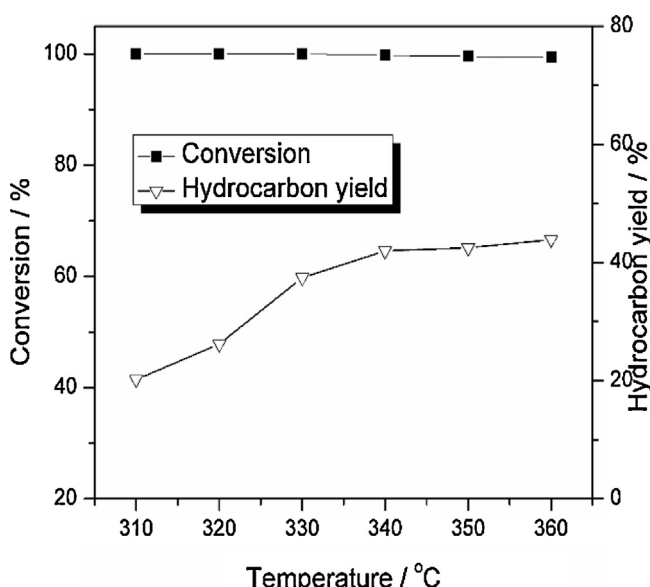


**Fig. 9.** Conversion of palmitic acid and hydrocarbon yield as a function of temperature over 40NiPZ. Experimental conditions: palmitic acid ( $1.5\text{ g}$ ), 40NiPZ ( $3.0\text{ g}$ ),  $P=0.1\text{ MPa}$ ,  $5\% \text{ H}_2/\text{Ar}$  with a flow rate of  $30\text{ mL min}^{-1}$ ,  $2.5\text{ h}$ .

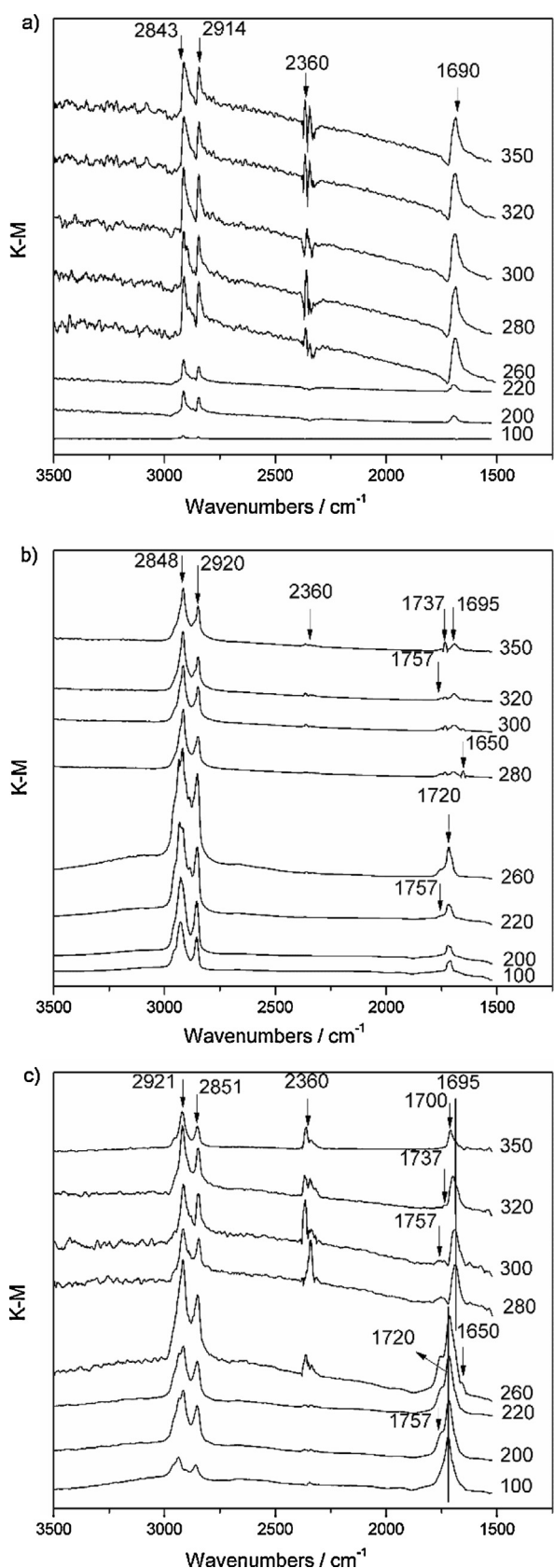


**Fig. 10.** *In situ* DRIFTS for the conversion of palmitic acid over unsupported Ni<sub>x</sub>P, HZSM-22, and 40NiPZ catalysts in the presence of 5% H<sub>2</sub>/Ar. (Temperature range from 100 to 350 °C).

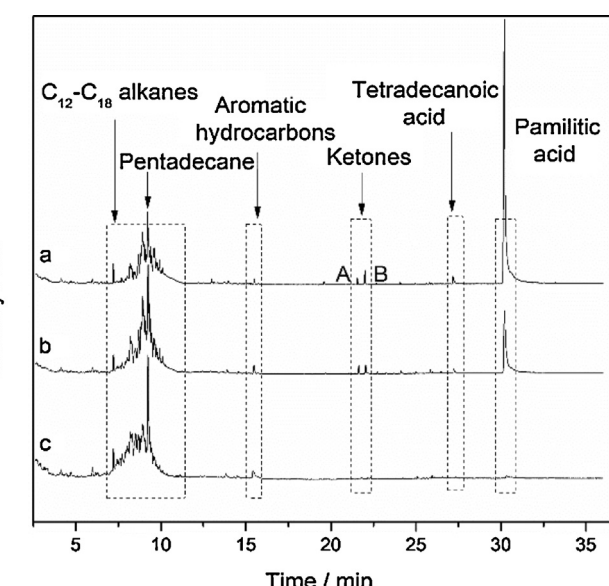


**Fig. 11.** GC chromatogram of the products formed from deoxygenation of palmitic acid over 40NiPZ at 350 °C with different catalyst dosages. (Catalyst dosage: a: 1 g; b: 2 g; c: 3 g. A: , B: ).

mainly composed of alkanes ( $C_{12}$ – $C_{18}$ ), aromatic hydrocarbons, ketones (five-membered ring ketones and long chain fatty ketones), tetradecanoic acid, and palmitic acid. Aldehydes and aromatic ketones were not observed, likely because of their instability and ease of conversion over 40NiPZ, thus confirming the results of *in situ* DRIFTS. By increasing the catalyst dosage, the amount of alkanes and aromatic hydrocarbons in the products also increased, whereas the amounts of ketones, tetradecanoic acid and palmitic acid decreased. When the catalyst dosage reached 3.0 g, ketones and fatty acids almost completely disappeared. Therefore, the results of the control experiments indicated that the reaction mechanism was complex and that the ketone intermediates were generated in the deoxygenation process, while the isomerization and cracking reactions also occurred in the conversion. All of these results are in good agreement with the *in situ* DRIFTS.

Based on the experimental results presented in the previous sections, the plausible deoxygenation pathways (**Scheme 2**) over 40NiPZ can be proposed as follows

a Decarbonylation. H<sub>2</sub> is first dissociated on Ni<sub>x</sub>P (Ni<sub>12</sub>P<sub>5</sub> and Ni<sub>2</sub>P) and the dissociated H combines with OH (in palmitic acid) to form H<sub>2</sub>O, generating C<sub>14</sub>H<sub>29</sub>-CH<sub>2</sub>-CHO (1757 cm<sup>-1</sup> in Fig. 10) as an intermediate. Finally, the intermediate is further converted to pentadecane by decarbonylation (Scheme 2a).

b Decarboxylation. Palmitic acid is directly converted into pentadecane by decarboxylation ([Scheme 2a](#)).  
 b Decarboxylation. Palmitic acid is directly converted into pentadecane by decarboxylation ( $2360\text{ cm}^{-1}$  in [Figs. 10 and 11](#)) ([Scheme 2b](#)).

c Isomerization and cracking. Isomerization and cracking can occur when palmitic acid directly interacts with Brønsted acid and Lewis acid sites on HZSM-22, respectively. First, OH (in palmitic acid) combines with H (in HZSM-22) and the C–C bands (in palmitic acid) are broken by the carbonium ion mechanism. Then,  $\text{H}_2\text{O}$  and ketones ( $1695, 1737 \text{ cm}^{-1}$  in Figs. 10 and 11) are formed, where the ketones can be converted into hydrocarbons via decarbonylation (Scheme 2c). Simultaneously, palmitic acid can be converted into aromatic hydrocarbons (or short chain hydrocarbons) and  $\text{C}_6\text{H}_4\text{-COOH}$  by cracking via isomerization. Finally,  $\text{C}_6\text{H}_4\text{-COOH}$  can be further converted into hydrocarbons by decarbonylation and decarboxylation (Scheme 2d).

The above plausible deoxygenation pathways might simultaneously occur and alter each other over 40NiPZ. The intermediates from decarbonylation and decarboxylation, such as pentadecane and  $C_{14}H_{29}-CH_2-CHO$  might undergo the isomerization and cracking reactions. The intermediates from the isomerization and cracking reactions, such as ketones and  $C_cH_d-COOH$ , might undergo further decarbonylation and decarboxylation. The hydrocarbons obtained resulted from the aggregation of the above processes.

#### 4. Conclusions

We have synthesized  $Ni_xP$  catalysts supported on commercial HZSM-22. The prepared  $Ni_xP/HZSM-22$  exhibited excellent catalytic activity, integrating deoxygenation, cracking and isomerization, for the conversion of palmitic acid to diesel-like hydrocarbons. The main products were  $C_{12}$ – $C_{18}$  alkanes, in addition to some aromatic hydrocarbons and cycloalkanes. With our supported catalysts, 40NiPZ, in a fixed-bed reactor under ambient pressure in the absence of any solvent, the conversion of palmitic acid was 99.6% and the hydrocarbon yield and the hydrocarbon heat value were 42.9% and  $46.4\text{ MJ kg}^{-1}$ , respectively. The crystalline phase of  $Ni_{12}P_5$  is proposed to be the main active phase in the deoxygenation of palmitic acid. The  $Ni_{12}P_5$  crystal size considerably affected the hydrocarbon yield, with the optimal size range identified as 20 to 24 nm for both the conversion of palmitic acid and the hydrocarbon yield. Various ketones and aldehydes were detected as the reaction intermediates, suggesting that the deoxygenation was accompanied by isomerization and cracking. The  $Ni_{12}P_5$  species of the 40NiPZ catalyst should be mainly responsible for the decarbonylation and decarboxylation, whereas Brønsted acid on HZSM-22 support should be largely responsible for the isomerization reactions and Lewis for the cracking reactions. Our study has demonstrated that the Ni-based catalysts supported on commercial HZSM-22 can convert saturated fatty acids into diesel-like hydrocarbons with high conversion, high hydrocarbon yield, and high hydrocarbon heat value.

#### Acknowledgements

This work was financially supported by the National Natural Science Foundation of China (No. 21303109) and the Application Foundation Program of Sichuan Province (No. 2013JY0007). We would also like to thank Professor Lin Dong's group of Nanjing University for *in situ* DRIFTS experiments.

#### Appendix A. Supplementary data

Supplementary data associated with this article can be found, in the online version, at <http://dx.doi.org/10.1016/j.apcatb.2015.03.023>.

#### References

- [1] E. Kunkes, D. Simonetti, R. West, J. Serrano-Ruiz, J. Dumesic, C. Gärtner, *Science* 322 (2008) 417–421.
- [2] C. Zhao, J. Lercher, *Angew. Chem.* 124 (2012) 6037–6042;
- [3] C. Zhao, J. Lercher, *Angew. Chem. Int. Ed.* (2012) 5935–5940.
- [4] M. Grilc, B. Likozar, J. Levec, *Appl. Catal. B: Environ.* 164 (2015) 48–60.
- [5] D. Kubická, J. Horáček, M. Setnická, R. Bulánek, A. Zukal, I. Kubicková, *Appl. Catal. B: Environ.* 145 (2014) 101–107.
- [6] T. Mochizuki, S.-Y. Chen, M. Toba, Y. Yoshimura, *Appl. Catal. B: Environ.* 146 (2014) 237–243.
- [7] (a) E. Santillan-Jimenez, T. Morgan, J. Lacny, S. Mohapatra, M. Crocker, *Fuel* 103 (2013) 1010–1017;
- [8] (b) E. Santillan-Jimenez, M. Croker, *J. Chem. Technol. Biotechnol.* 87 (2012) 1041–1050.
- [9] C. Wang, Z. Tian, L. Wang, R. Xu, Q. Liu, W. Qu, H. Ma, B. Wang, *ChemSusChem* 5 (2012) 1974–1983.
- [10] J. Immer, M. Kelly, H. Lamb, *Appl. Catal. A: Gen.* 375 (2010) 134–139.
- [11] B. Peng, C. Zhao, S. Kasakov, S. Foraita, J. Lercher, *Chem. Eur. J.* 19 (2013) 4732–4741.
- [12] P. Mäki-Arvela, I. Kubičková, M. Snáre, K. Eränen, D. Murzin, *Energy Fuels* 21 (2007) 30–41.
- [13] I. Simakova, B. Rozmysłowicz, O. Simakova, P. Mäki-Arvela, A. Simakov, D. Murzin, *Top. Catal.* 54 (2011) 460–466.
- [14] M. Snáre, I. Kubičková, P. Mäki-Arvela, D. Chichova, K. Eränen, D. Murzin, *Fuel* 87 (2008) 933–945.
- [15] M. Snáre, I. Kubičková, P. Mäki-Arvela, K. Eränen, D. Murzin, *Ind. Eng. Chem. Res.* 45 (2006) 5708–5715.
- [16] J. Fu, X. Lu, P. Savage, *ChemSusChem* 4 (2011) 481–486.
- [17] T. Morgan, D. Grubb, E. Santillan-Jimenez, M. Croker, *Top. Catal.* 53 (2010) 820–829.
- [18] (a) K. Li, R. Wang, J. Chen, *Energy Fuels* 25 (2011) 854–863;
- [19] (b) J.A. Cecilia, A. Infantes-Molina, E. Rodríguez-Castellón, A. Jiménez-López, S.T. Oyama, *Appl. Catal. B: Environ.* 136–137 (2013) 140–149.
- [20] Y. Yang, C. Ochoa-Hernández, V. de la Peña O'shea, J. Coronado, D.P. Serrano, *ACS Catal.* 2 (2012) 592–598.
- [21] Y. Zeng, B. Zhao, L. Zhu, D. Tong, C. Hu, *RSC Adv.* 3 (2013) 10806–10816.
- [22] Y. Zhao, M. Xue, M. Cao, J. Shen, *Appl. Catal. B: Environ.* 104 (2011) 229–233.
- [23] D. Kubíčka, M. Bejblová, J. Vlk, *Top. Catal.* 53 (2010) 168–178.
- [24] S. Sawhill, D. Phillips, M. Bussell, *J. Catal.* 215 (2003) 208–219.
- [25] S. Sawhill, K. Layman, D. Van Wyk, M. Engelhard, C. Wang, M. Bussell, *J. Catal.* 231 (2005) 300–313.
- [26] T. Chen, B. Yang, S. Li, K. Wang, X. Jiang, Y. Zhang, G. He, *Ind. Eng. Chem. Res.* 50 (2011) 11043–11048.
- [27] (a) S. Xu, X. Wang, *Fuel* 84 (2005) 563–567;
- [28] (b) J. Chen, H. Shi, L. Li, K. Li, *Applied Catalysis B: Environ.* 144 (2014) 870–884.
- [29] S. Kirumakki, B. Sheizer, G. Vidya Sagar, K. Chary, A. Clearfield, *J. Catal.* 242 (2006) 319–331.
- [30] C. Wagner, Practical Surface Analysis by Auger and X-ray Photoelectron Spectroscopy, in: D. Briggs, M. Seah (Eds.), John Wiley & Sons, New York, 1983, p. 495.
- [31] T. Korányi, Z. Vit, D. Poduval, R. Ryoo, H. Seung Kim, E. Hensen, *J. Catal.* 253 (2008) 119–131.
- [32] T. Korányi, *Appl. Catal. A: Gen.* 239 (2003) 253–267.
- [33] (a) P. Larkin, Infrared and Raman Spectroscopy Principles and Spectral Interpretation, Elsevier, Oxford, 2011, pp. 60–215;
- [34] (b) J. Naktiyok, H. Bayrakçeken, A. Özer, M. Gülaboğlu, *Fuel Process. Technol.* 116 (2013) 158–164.
- [35] D. Li, Q. Yu, S. Li, H. Wan, L. Liu, L. Qi, B. Liu, F. Gao, L. Dong, Y. Chen, *Chem. Eur. J.* 17 (2011) 5668–5679.